Improved Solid Oxide Fuel Cell Performance with Nanostructured Electrolytes

Cheng-Chieh Chao,[†] Ching-Mei Hsu,[‡] Yi Cui,[‡] and Fritz B. Prinz[†,‡,*]

[†]Department of Mechanical Engineering and [‡]Department of Materials Science and Engineering, Stanford University, Building 530, 440 Escondido Mall, California 94305, United States

ABSTRACT Considerable attention has been focused on solid oxide fuel cells (SOFCs) due to their potential for providing clean and reliable electric power. However, the high operating temperatures of current SOFCs limit their adoption in mobile applications. To lower the SOFC operating temperature, we fabricated a corrugated thin-film electrolyte membrane by nanosphere lithography and atomic layer deposition to reduce the polarization and ohmic losses at low temperatures. The resulting micro-SOFC electrolyte membrane showed a hexagonal-pyramid array nanostructure and achieved a power density of 1.34 W/cm^2 at 500 °C. In the future, arrays of micro-SOFCs with high power density may enable a range of mobile and portable power applications.

KEYWORDS: atomic layer deposition · yttria-stabilized zirconia · solid oxide fuel cells · micro solid oxide fuel cells · nanosphere lithography

Solid oxide fuel cells (SOFCs) are attractive because of their high energy conversion efficiency in the usage of fuels ranging from hydrogen to hydrocarbons.[1−6] Nevertheless, they have limited applications because this high efficiency requires high operating temperatures, which pose significant engineering challenges, diminishing the SOFCs practicality for applications such as portable power sources. Lowering the operating temperatures of SOFCs would improve thermal stability and offer shorter start-up times, which in turn would broaden their use as auxiliary power units for automobiles.[7−9] Although many studies have aimed at lowering SOFC operating temperatures, the resulting temperature reduction has been inevitably accompanied by a decrease in ionic conduction of the electrolyte and power density.

One approach to improving SOFC performance at lower temperatures is to introduce electrolyte materials with higher ionic conductivity. A candidate for a low- or intermediate-temperature SOFC electrolyte is the $La_{0.9}Sr_{0.1}Ga_{0.8}Mg_{0.2}O_{3-\delta}$ (LSGM) electrolyte, which has been demonstrated to significantly improve the maximum power density of the SOFC to 0.612 W/cm^2 at 500 °C.[10] Another candidate is the $Sm_{0.075}Nd_{0.075}Ce_{0.85}O_{2-\delta}$ (SNDC) electrolyte, which also has been demonstrated to improve the maximum power density to 0.32 W/cm^2 at 500 °C.[11] These electrolytes exhibit high ionic conductivity; however, they are less stable than yttria-stabilized zirconia (YSZ).

A second approach to improving SOFC performance is to reduce electrolyte thickness. Recent studies in micro-SOFCs demonstrated enhanced reaction and transport kinetics at relatively low temperatures (300−500 °C),[12−17] indicating that high power density, low-temperature SOFC devices may be feasible. The use of microelectromechanical system (MEMS) processing allows fabrication of micrometer-thick freestanding SOFC electrolytes, which reduce ohmic losses during fuel cell operations. These microscale zirconia- and ceria-based electrolytes are typically deposited by physical vapor deposition techniques that produce high-quality thin films with few pinholes.[18] In our recent study, instead of using physical vapor deposition techniques in our micro-SOFC fabrication process, we adopted atomic layer deposition (ALD), a chemical vapor deposition technique that allows reducing the YSZ electrolyte thickness to tens of nanometers.[19−21] With such thin electrolytes, ohmic losses are no longer rate-controlling, thereby making polarization losses the dominant loss mechanism for fuel cell performance.

In general, reducing current density in a fuel cell reduces polarization losses, although lowering the power output. By increasing the area of the electrolyte membrane one can compensate for the reduced power output. For that purpose we fabricated three-dimensional corrugated thin-film electrolytes in a previous study with a surface area five times greater than a noncorrugated electrolyte by using an extensive number of photolithography steps.[22] The resulting

* Address correspondence to fprinz@stanford.edu.

Received for review April 12, 2011 and accepted June 9, 2011.

Published online June 09, 2011
10.1021/nn201354p

maximum power densities of these fuel cells reached 0.861 W/cm^2 at 450 °C. However, the fabrication complexity rendered this approach costly and difficult.

In the present study, we describe a method for fabricating corrugated electrolyte membranes with a reduced fabrication complexity. We used a wafer-scale self-assembly nanotexturing technique to pattern the surfaces of our ALD YSZ electrolytes, applying nanosphere lithography (NSL) to create a three-dimensional pattern on a silicon substrate.[23−25] Due to the self-assembly characteristics of nanospheres, we were able to form close-packed patterns without resorting to conventional lithography steps that require mask design and fabrication, followed by photoresist application, development, and removal. The geometry of this nanostructured pattern was determined by the dry etching conditions of the process. To replicate this three-dimensional nanostructured geometry with increased surface area, we coated the patterned substrate with an YSZ electrolyte using ALD. This ALD coating was composed of zirconia doped with 7−8 mol % of yttria and provided a pinhole-free and conformal electrolyte throughout the entire active fuel cell area. Depositing ultrathin pinhole-free conformal coatings over corrugated geometries is unique to ALD processing;[26,27] similar coatings are difficult if not impossible to achieve with physical vapor deposition methods.

RESULTS AND DISCUSSION

Figure 1 shows a schematic of the membrane electrode assembly (MEA) design and the scanning electron microscope (SEM) images of the nanostructured MEA. The dimensions of the freestanding MEA area are 100 μm by 100 μm, with a surrounding silicon structure supporting the membrane. The SEM images demonstrate the feasibility of fabricating MEAs with a close-packed array of hexagonal pyramids. The sides of these hexagonal pyramids were approximately 800 nm, and the height of the pyramids approximately 800 nm, providing a corrugated area 1.6−2 times larger than the projected area of the planar structure. The final electrolyte thickness was 80 nm, and the electrode thickness was 60 nm, which resulted in an ultrathin freestanding platinum/YSZ/platinum MEA with a thickness of 200 nm. The SEM mircrographs obtained after electrochemical characterizations exhibited no change in the electrolyte nanostructure. However, consistent with earlier observations,[28,29] indications of platinum coalescence in the electrode texture were noticed.

During fuel cell performance characterization, the anode side of the fuel cell was sealed to a heated hydrogen flow chamber, exposing that side to a 10 sccm flow of pure hydrogen. The cathode side of the fuel cell was exposed to the atmosphere without external heating. The dense and pinhole-free ALD YSZ electrolyte prevented fuel crossover, thereby eliminating the

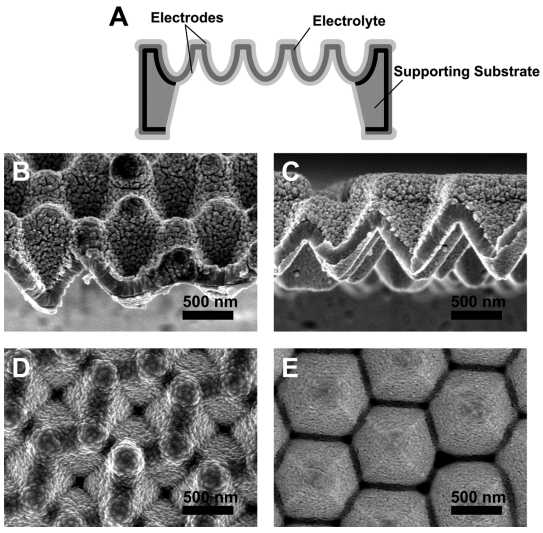

Figure 1. (A) Schematic of the freestanding platinum/YSZ/platinum MEA design. (B) SEM image of the nanostructured MEA with porous platinum electrodes and an ALD YSZ electrolyte obtained after electrochemical characterizations. (C) Side view of the MEA. (D) Top view from the cathode side. (E) Bottom view from the anode side. The thickness of the MEA was approximately 200 nm.

leakage current through the electrolyte. In addition, the electrolyte was sufficiently thin that ohmic losses could be neglected for small currents. As a result, the measured open-circuit voltages (OCV) of the micro-SOFC were close to the theoretical values derived from the Nernst equation, reaching 1.14, 1.11, and 1.10 V at 400, 450, and 500 °C, respectively.

Figure 2A shows the impedance spectra of the nanostructured MEA and the unpatterned MEA at 450 °C. The high-frequency (200 kHz) intercepts, corresponding to the ohmic resistances of the MEAs, were approximately 0.05 Ω cm^2. The extrapolated electrolyte conductivities for both MEAs were approximately 2×10^{-4} S/cm at 450 °C, similar to the YSZ conductivity reported in the literature.[30−32] Despite the additional patterning process used in the nanostructured MEA, the ohmic resistance remained unaffected by the difference in the electrolyte geometries. However, the low frequency (0.1 Hz) interceptions, corresponding to the polarization resistances of the MEAs, were strongly affected by the MEA geometries. The polarization resistance of the nanostructured MEA was approximately 30% less than the resistance of the unpatterned MEA at this temperature, reflecting the change in the cathode/electrolyte interfacial area. This can also be observed in Figure 2B, where polarization losses are affected by the geometries of the MEAs. We believe this electrochemical performance enhancement is due to the increase in the electrochemically active interfacial area resulting from the corrugation.

The current−voltage performances of the nanostructured micro-SOFC at different temperatures are shown in Figure 3. The maximum power per cell is

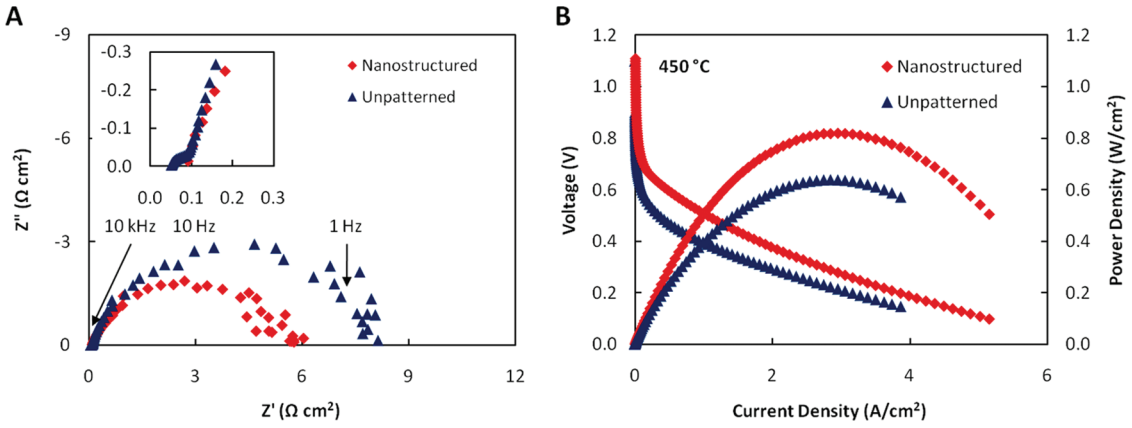

Figure 2. (A) Impedance spectra of the nanostructured MEA and the unpatterned MEA under open-circuit voltage conditions at 450 °C. (B) Current–voltage performances of the nanostructured MEA and the unpatterned MEA using pure hydrogen fuel at 450 °C. The maximum power densities of the nanostructured MEA and the unpatterned MEA at 450 °C are 0.82 and 0.56 W/cm^2, respectively.

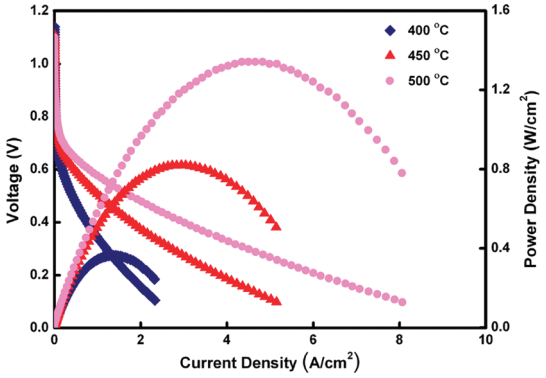

Figure 3. Fuel cell performance of the three-dimensional nanostructured MEA at 400, 450, and 500 °C. The maximum power densities are 0.36, 0.82, and 1.34 W/cm^2, respectively.

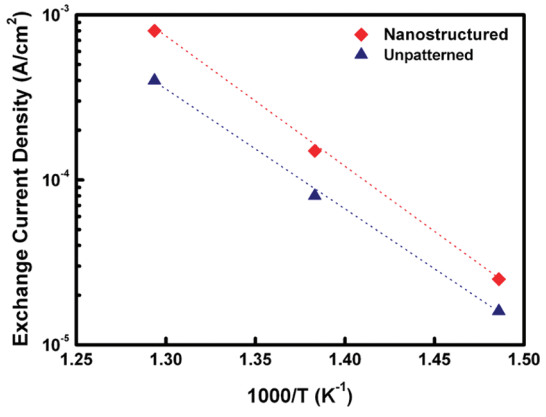

Figure 4. Exchange current densities of the nanostructured MEA and the unpatterned MEA. This enhancement was attained by increasing the cathode/electrolyte interfacial area of the MEA.

36, 82, and 134 μW at 400, 450, and 500 °C, with a projected area of 10^{-4} cm^2 in each cell. The maximum power of the unpatterned cell with the same projected area is 24, 56, and 90 μW, respectively. Reducing the electrolyte thickness and increasing the cathode/electrolyte

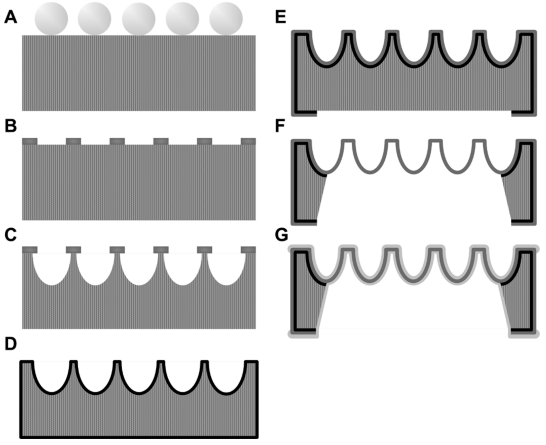

Figure 5. Fabrication process of a 3D nanostructured electrolyte: (A) Transfer silica nanoparticles onto a silicon substrate *via* the Langmuir–Blodgett method and perform etching to control the nanoparticle size. (B) Sputter aluminum on the sample and remove the nanoparticles, creating a metal mask. (C) Etch the sample to form a three-dimensional nanoscale pattern. (D) Remove the metal mask by wet etching. Deposit silicon nitride as an etch barrier. (E) Define the fuel cell window by patterning the silicon nitride on the back side. Deposit the ALD YSZ electrolyte on the front side. (F) Remove silicon by wet etching and the silicon nitride by dry etching. (G) Sputter porous platinum electrodes.

interfacial area have significantly improved fuel cell performance at these temperatures. However, these current–voltage curves still indicate notable polarization losses, which may be further reduced by using materials with higher catalytic activities relative to YSZ. The maximum power density of both cells after 1 h at 500 °C decreased to 80% due to platinum coalescence at elevated temperatures. Similar electrochemical performance degradation was reported by Kerman *et al.* with a comparable experimental setup.[28] Electrode materials may be replaced by alloys, such as platinum–nickel,[29] or ceramic materials, such as lanthanum strontium cobalt iron oxide,[30] to improve thermal stability of the electrode and offset the high cost of platinum.

In Figure 4, we compare the exchange current density of the nanostructured MEA and the unpatterned MEA at three different temperatures. The observed exchange current densities are higher compared with previously reported data.[31] We attribute this gain to the surface characteristics of nanogranular YSZ films, as reported by Shim and Huang from our laboratory.[19,33] Their studies suggest that nanogranular films show higher surface exchange coefficients and increased exchange density at the platinum/nanogranular−YSZ interface. As shown in Figure 4, the exchange current density as normalized by the projected area reflects the increase in the corrugated surface area.

To conclude, we demonstrated that the nanostructured electrolyte provided a considerably larger surface area compared with the unpatterned electrolyte, ultimately resulting in a higher power density per projected area. We were able to achieve a maximum power density of 1.34 W/cm^2 at 500 °C by combining a surface patterning technique with ALD despite using an YSZ electrolyte with low ionic conductivity at this temperature. This study focuses on achieving maximizing power density; the absolute power output of the reported structure is low due to the size of the active area. The methodology appears applicable to larger areas. The adoption of nanosphere lithography reduces the number of photolithography steps required to create three-dimensional patterns, thereby simplifying the process for fabricating three-dimensional nanostructured micro-SOFCs. The present cell architecture offers the prospects of realizing power systems with micro-SOFC arrays for mobile power sources with high power and high power density operating below 500 °C.

METHODS

Sample Preperation. Figure 5 shows the process flow used to fabricate a three-dimensional nanostructured template. First, silica nanoparticles were synthesized following the Stöber method.[34,35] The surfaces of these nanoparticles were modified by 3-aminopropyl methyl diethoxysilane to control the hydrophobicity of particles and prevent particle aggregation.[36] The nanoparticles were then transferred onto a 4-inch silicon substrate *via* the Langmuir−Blodgett method to deposit a monolayer of close-packed nanoparticles on the substrate. To introduce spacing between the close-packed nanoparticles, fluorine-based reactive ion etching was applied to reduce the diameter of the nanoparticles. To fabricate the nanostructure, 100 nm of aluminum was subsequently sputtered on top of the etched pattern to create a metal mask with an inverse pattern of the nanoparticles, which were then removed by sonication in ethanol. After fabrication of the mask, the substrate was dry-etched with a mixture of sulfur hexafluoride and chlorodifluoromethane, creating nanometer-sized trenches on the substrate, the geometry of which was determined by etching time, power, chemical flow rate, and chamber pressure. The remaining metal mask was removed by wet chemical etch, leaving a silicon substrate with a three-dimensional nanostructured surface.

We used ALD to fabricate the electrolyte membrane consisting of YSZ with 7−8 mol % yttria doping. This was done by sequentially depositing seven layers of zirconia and one layer of yttria. We adopted tetrakis(dimethylamido)zirconium and tris-(methylcyclopentadienyl)yttrium as precursors and distilled water as oxidant. The substrate was heated to 250 °C during deposition. The time required for each ALD cycle was 60 s, and 1000 cycles were needed per membrane. A detailed account of ALD YSZ is given in an earlier report.[19]

This nanoscale YSZ electrolyte was then deposited on the patterned substrate by ALD, replicating the nanostructured pattern from the substrate. The supporting silicon substrate was removed by wet etching, leaving a freestanding nanostructured ALD YSZ electrolyte. Porous platinum, serving as both electrodes and catalyst, was subsequently sputtered on both sides of the electrolyte. A detailed description of the fuel cell fabrication process is available in a previous publication.[17]

Characterization. During fuel cell performance characterization, the anode side of the fuel cell was sealed to a small stainless steel hydrogen flow chamber with a gold ring, the cathode side was connected to a gold probe tip for current collection using a micromanipulator, and the electrochemical measurements were performed with a Gamry femtostat. The hydrogen chamber was heated with a 1-inch button heater (HeatWave Laboratories), while the temperature of the heater was measured with a thermocouple (type K, HeatWave Laboratories). We verified that the surface temperature of the cathode was below the heater temperature by taking advantage of the melting points of tin and zinc shots (99.999%, 3 mm, Sigma-Aldrich) at 232 and 420 °C, respectively. Independent of the melting points, the temperature of the heated chamber, as measured with an infrared thermometer (Fluke), was determined to be 10−20 °C lower than the heater temperature due to air cooling. From these temperature measurements, we conclude that the fuel cell operating temperature was close to if not lower than the heater temperature.

The impedance spectra were acquired using a Gamry femtostat under OCV conditions with frequency scanning from 200 kHz to 0.1 Hz, which showed a high-frequency intersection and a low-frequency arc. The high-frequency intersection was insensitive to the dc bias applied to the fuel cell, while the low-frequency arc changed according to the bias. This indicates that the high-frequency intersection and the low-frequency arc correspond to the electrolyte resistance and the interfacial resistance, respectively. Similar phenomena with thin film electrolytes were also reported by Huang *et al.*[17]

The exchange current density (j_0) was extrapolated by fitting polarization loss ($\eta_{polarization}$) and current response (j) in the fuel cell current−voltage data using the Tafel equation:

$$\eta_{polarization} = \frac{RT}{\alpha nF} \ln \frac{j}{j_0}$$

where R is the gas constant, T is the absolute temperature, α is the charge transfer coefficient, n is the number of electrons involved in the electrode reaction, and F is the Faraday constant.

Polarization loss is estimated by deducting ohmic loss from overpotential. As no indication of concentration loss was observed in the current−voltage curve, we did not consider concentration loss in determining exchange current density. Overpotential is directly acquired from the current−voltage data, and ohmic loss is estimated from the electrolyte resistance times current.

Acknowledgment. C.-C.C. and F.B.P. acknowledge support from Honda. T. M. Gür, J. Schoonman, J. H. Shim, and P.-C. Su contributed to this research through discussions. Y.C. acknowledges support from the DOE-EFRC: CNEEC (Award No. DE-SC0001060). ALD reactors in our laboratory were built with support from CNEEC.

REFERENCES AND NOTES

1. Steele, B. C. H.; Heinzel, A. Materials for Fuel-Cell Technologies. *Nature* **2001**, *414*, 345–352.
2. Yamamoto, O. Solid Oxide Fuel Cells: Fundamental Aspects and Prospects. *Electrochim. Acta* **2000**, *45*, 2423–2435.
3. Minh, N. Q. Solid Oxide Fuel Cell Technology—Features and Applications. *Solid State Ionics* **2004**, *174*, 271–277.
4. Park, S.; Vohs, J. M.; Gorte, R. J. Direct Oxidation of Hydrocarbons in a Solid-Oxide Fuel Cell. *Nature* **2000**, *404*, 265–267.
5. Hibino, T.; Hashimoto, A.; Asano, K.; Yano, M.; Suzuki, M.; Sano, M. An Intermediate-Temperature Solid Oxide Fuel Cell Providing Higher Performance with Hydrocarbons than with Hydrogen. *Electrochem. Solid-State Lett.* **2002**, *5*, A242–A244.
6. Stambouli, A. B.; Traversa, E. Solid Oxide Fuel Cells (SOFCs): A Review of an Environmentally Clean and Efficient Source of Energy. *Renewable Sustainable Energy Rev.* **2002**, *6*, 433–455.
7. Singhal, S. C. Solid Oxide Fuel Cells for Stationary, Mobile, and Military Applications. *Solid State Ionics* **2002**, *152*, 405–410.
8. Lamp, P.; Tachtler, J.; Finkenwirth, O.; Mukerjee, S.; Shaffer, S. Development of an Auxiliary Power Unit with Solid Oxide Fuel Cells for Automotive Applications. *Fuel Cells* **2003**, *3*, 146–152.
9. Shao, Z.; Haile, S. M.; Ahn, J.; Ronney, P. D.; Zhan, Z.; Barnett, S. A. A Thermally Self-sustained Micro Solid-Oxide Fuel-Cell Stack with High Power Density. *Nature* **2005**, *435*, 795–798.
10. Yan, J.; Matsumoto, H.; Enoki, M.; Ishihara, T. High-Power SOFC Using $La_{0.9}Sr_{0.1}Ga_{0.8}Mg_{0.2}O_{3-\delta}/Ce_{0.8}Sm_{0.2}O_{2-\delta}$ Composite Film. *Electrochem. Solid-State Lett.* **2005**, *8*, A389–A391.
11. Ahn, J. S.; Omar, S.; Yoon, H.; Nino, J. C.; Wachsman, E. D. Performance of Anode-supported Solid Oxide Fuel Cell Using Novel Ceria Electrolyte. *J. Power Sources* **2010**, *195*, 2131–2135.
12. De Souza, S.; Visco, S. J.; De Jonghe, L. C. Reduced-Temperature Solid Oxide Fuel Cell Based on YSZ Thin-Film Electrolyte. *J. Electrochem. Soc.* **1997**, *144*, L35–L37.
13. Will, J.; Mitterdorfer, A.; Kleinlogel, C.; Perednis, D.; Gauckler, L. J. Fabrication of Thin Electrolytes for Second-Generation Solid Oxide Fuel Cells. *Solid State Ionics* **2000**, *131*, 79–96.
14. Baertsch, C. D.; Jensen, K. F.; Hertz, J. L.; Tuller, H. L.; Vengallatore, S. T.; Spearing, S. M.; Schmidt, M. A. Fabrication and Structural Characterization of Self-Supporting Electrolyte Membranes for a Micro Solid-Oxide Fuel Cell. *J. Mater. Res.* **2004**, *19*, 2604–2615.
15. Chen, X.; Wu, N. J.; Smith, L.; Ignatiev, A. Thin-Film Heterostructure Solid Oxide Fuel Cells. *Appl. Phys. Lett.* **2004**, *84*, 2700–2702.
16. Srikar, V. T.; Turner, K. T.; Ie, T. Y.; Spearing, S. M. Structural Design Considerations for Micromachined Solid-Oxide Fuel Cells. *J. Power Sources* **2004**, *125*, 62–69.
17. Huang, H.; Nakamura, M.; Su, P.-C.; Fasching, R.; Saito, Y.; Prinz, F. B. High-Performance Ultrathin Solid Oxide Fuel Cells for Low-Temperature Operation. *J. Electrochem. Soc.* **2007**, *154*, B20–B24.
18. Negishi, A.; Nozaki, K.; Ozawa, T. Thin-Film Technology for Solid Electrolyte Fuel Cells by the RF Sputtering Technique. *Solid State Ionics* **1981**, *3*, 443–446.
19. Shim, J. H.; Chao, C.-C.; Huang, H.; Prinz, F. B. Atomic Layer Deposition of Yttria-Stabilized Zirconia for Solid Oxide Fuel Cells. *Chem. Mater.* **2007**, *19*, 3850–3854.
20. Ginestra, C.; Sreenivasan, R.; Karthikeyan, A.; Ramanathan, S.; McIntyre, P. C. Atomic Layer Deposition of Y_2O_3/ZrO_2 Nanolaminates. *Electrochem. Solid-State Lett.* **2007**, *10*, B161–B165.
21. Cassir, M.; Ringuedé, A.; Niinistö, L. Input of Atomic Layer Deposition for Solid Oxide Fuel Cell Applications. *J. Mater. Chem.* **2010**, *20*, 8987–8993.
22. Su, P.-C.; Chao, C.-C.; Shim, J. H.; Fasching, R.; Prinz, F. B. Solid Oxide Fuel Cell with Corrugated Thin Film Electrolyte. *Nano Lett.* **2008**, *8*, 2289–2292.
23. Deckman, H. W.; Dunsmuir, J. H. Natural Lithography. *Appl. Phys. Lett.* **1982**, *41*, 377–379.
24. Haynes, C. L.; Van Duyne, R. P. Nanosphere Lithography: A Versatile Nanofabrication Tool for Studies of Size-Dependent Nanoparticle Optics. *J. Phys. Chem. B* **2001**, *105*, 5599–5611.
25. Hsu, C.-M.; Connor, S. T.; Tang, M. X.; Cui, Y. Wafer-Scale Silicon Nanopillars and Nanocones by Langmuir–Blodgett Assembly and Etching. *Appl. Phys. Lett.* **2008**, *93*, 133109–133111.
26. Ritala, M.; Leskelä, M. Atomic Layer Epitaxy – a Valuable Tool for Nanotechnology? *Nanotechnology* **1999**, *10*, 19–24
27. George, S. M. Atomic Layer Deposition: An Overview. *Chem. Rev.* **2010**, *110*, 111–131.
28. Kerman, K.; Lai, B.-K.; Ramanatham, S. $Pt/Y_{0.16}Zr_{0.84}O_{1.92}/Pt$ Thin Film Solid Oxide Fuel Cells: Electrode Microstructure and Stability Considerations. *J. Power Sources* **2011**, *196*, 2608.
29. Wang, X.; Huang, H.; Holme, T.; Tian, X.; Prinz, F. B. Thermal Stabilities of Nanoporous Metallic Electrodes at Elevated Temperatures. *J. Power Sources* **2007**, *175*, 75–81.
30. Johnson, A. C.; Lai, B.-K.; Xiong, H.; Ramanathan, S. An Experimental Investigation into Micro-fabricated Solid Oxide Fuel Cells with Ultra-Thin $La_{0.6}Sr_{0.4}Co_{0.8}Fe_{0.2}O_3$ Cathodes and Yttria-Doped Zirconia Electrolyte Films. *J. Power Sources* **2009**, *186*, 252–260.
31. Steele, B. C. H. Interfacial Reactions Associated with Ceramic Ion Transport Membranes. *Solid State Ionics* **1995**, *75*, 157–165.
32. Kosacki, I.; Rouleau, C. M.; Becher, P. F.; Bentley, J.; Lowndes, D. H. Nanoscale Effects on the Ionic Conductivity in Highly Textured YSZ Thin Films. *Solid State Ionics* **2005**, *176*, 1319–1326.
33. Huang, H.; Shim, J. H.; Chao, C.-C.; Pornprasertsuk, R.; Sugawara, M.; Gür, T. M.; Prinz, F. B. Characteristics of Oxygen Reduction on Nanocrystalline YSZ. *J. Electrochem. Soc.* **2009**, *156*, B392–B396.
34. Bogush, G. H.; Tracy, M. A.; Zukoski, C. F., IV. Preparation of Monodisperse Silica Particles: Control of Size and Mass Fraction. *J. Non-Cryst. Solids* **1988**, *104*, 95–106.
35. Stöber, W.; Fink, A.; Bohn, E. Controlled Growth of Monodisperse Silica Spheres in the Micron Size Range. *J. Colloid Interface Sci.* **1968**, *26*, 62–69.
36. Wu, Z.; Xiang, H.; Kim, T.; Chun, M.-S.; Lee, K. Surface Properties of Submicrometer Silica Spheres Modified with Aminopropyltriethoxysilane and Phenyltriethoxysilane. *J. Colloid Interface Sci.* **2006**, *304*, 119–124.